Title

Overexpression of calcium-activated potassium channels underlies cortical dysfunction in a model of PTEN-associated autism

Journal

Proceedings of the National Academy of Sciences of the United States of America, 110(45)

ISSN

0027-8424

Authors

Garcia-Junco-Clemente, Pablo
Chow, David K
Tring, Elaine
et al.

Publication Date

2013-11-05

DOI

10.1073/pnas.1309207110

Peer reviewed

Overexpression of calcium-activated potassium channels underlies cortical dysfunction in a model of *PTEN*-associated autism

Pablo Garcia-Junco-Clemente[a,1], David K. Chow[a,1], Elaine Tring[a], Maria T. Lazaro[b], Joshua T. Trachtenberg[a], and Peyman Golshani[b,2]

Departments of [a]Neurobiology and [b]Neurology, David Geffen School of Medicine at UCLA, Los Angeles, CA 90095

Edited by Bernardo Sabatini, Harvard Medical School, Boston, MA, and accepted by the Editorial Board September 25, 2013 (received for review May 15, 2013)

De novo phosphatase and tensin homolog on chromosome ten (*PTEN*) mutations are a cause of sporadic autism. How single-copy loss of *PTEN* alters neural function is not understood. Here we report that *Pten* haploinsufficiency increases the expression of small-conductance calcium-activated potassium channels. The resultant augmentation of this conductance increases the amplitude of the afterspike hyperpolarization, causing a decrease in intrinsic excitability. In vivo, this change in intrinsic excitability reduces evoked firing rates of cortical pyramidal neurons but does not alter receptive field tuning. The decreased in vivo firing rate is not associated with deficits in the dendritic integration of synaptic input or with changes in dendritic complexity. These findings identify calcium-activated potassium channelopathy as a cause of cortical dysfunction in the *PTEN* model of autism and provide potential molecular therapeutic targets.

gain | visual cortex | SK | mTOR | sensory processing

Children with inherited or de novo mutations in a single copy of phosphatase and tensin homolog on chromosome ten (*PTEN*) show symptoms of autism, macrocephaly, mental retardation, and epilepsy (1–3), and de novo *PTEN* mutations are one of the most validated causes of autism (4). This interest has led to the development of a number of lines of mutant mice with conditional homozygous *Pten* deletion in forebrain neurons. These mice are macrocephalic and epileptic and display abnormal social interactions and exaggerated responses to sensory stimuli (5, 6). Because these mice display behavioral deficits that are also seen in autistic children, a number of studies have examined cortical connectivity and synaptic strength following *Pten* gene deletion and found enlarged neural somata, overgrown dendrites, and hyperconnected neural networks (5–8). These studies and studies in other mouse lines bearing mutations found in autistic individuals (9, 10) identify deficits in synaptic strength and number as the major etiology of abnormal circuit function in autism.

Alternatively, or in addition, cortical dysfunction in autism may be driven by changes in the normal expression of voltage-sensitive and/or calcium-activated ion conductances, which would alter neural excitability. Supporting this view, calcium channelopathy causes Timothy syndrome where 80% of individuals surviving past the age of three are autistic (11). Common and rare mutations in *CNTNAP2*, the protein product of which clusters voltage-sensitive potassium channels at the juxtaparanode of axons, are also strongly associated with autism (12–14), as are mutations in *SCN2A* (15), which codes the α-subunit of a voltage-gated sodium channel.

The AKT/mTOR-signaling pathway that is regulated by PTEN regulates the translation Kv1.1 voltage-gated potassium channels (16). Whether *Pten* mutation impacts the expression of other ion channels that regulate neural excitability is not known. Nor is it understood how *Pten* mutation impacts the processing of sensory information in vivo. Sensory-processing deficits are found in 80–90% of autistic individuals and may underlie some of the behavioral problems associated with autism.

Here we focus our studies on mice lacking one copy of *Pten* because heterozygous mutation more accurately models the human disease, whereas double-copy loss is lethal. Using two-photon imaging to target cell-attached and whole-cell recordings to layer 2/3 (L2/3) pyramidal neurons in the primary visual cortex, we find that single-copy loss reduces stimulus-evoked firing rates by half of their control values but has no impact on the selectivity of evoked firing to stimulus orientation and direction. Notably, the amplitude of subthreshold voltage responses to optimal visual stimuli was not different from controls. The reduction in neural firing is caused by increased expression of small-conductance calcium-activated potassium (SK_{Ca}) channels, which limit the firing frequency of neurons by regulating the action potential after hyperpolarization.

These results identify an unsuspected mechanism by which PTEN regulates cortical gain control in vivo, thereby altering sensory processing.

Results

PTEN regulates many aspects of cortical development, including proliferation, survival, migration, differentiation, lamination, and dendritic growth, as well as synaptic connectivity (8, 17). To examine PTEN's role in regulating neural plasticity and sensory processing, we recorded from L2/3 pyramidal neurons in the mouse primary visual cortex in *Pten* conditional knockout mice and wild-type controls. Neurons in the mouse visual cortex have

Significance

Advances in human genetics have identified many gene alterations that cause autism, but how these mutations lead to cortical dysfunction is not understood. Mutations in the gene phosphatase and tensin homolog on chromosome ten (*PTEN*) cause autism and intellectual disability. We have discovered that single-copy deletion of *Pten* results in overexpression of the small-conductance calcium-activated potassium channel in cortical neurons. This overexpression leads to decreased sensitivity of cortical neurons to incoming inputs. In vivo, this diminished excitability leads to decreased primary visual cortical responsiveness to visual stimuli. We hypothesize that diminished cortical responses in primary sensory regions lead to poor recruitment of secondary sensory cortices, leading to sensory processing deficits. Our findings identify a unique target for potential pharmacological intervention.

Author contributions: P.G.-J.-C., D.K.C., J.T.T., and P.G. designed research; P.G.-J.-C., D.K.C., E.T., M.T.L., J.T.T., and P.G. performed research; P.G.-J.-C., D.K.C., E.T., M.T.L., J.T.T., and P.G. analyzed data; and P.G.-J.-C., D.K.C., J.T.T., and P.G. wrote the paper.

The authors declare no conflict of interest.

This article is a PNAS Direct Submission. B.S. is a guest editor invited by the Editorial Board.

[1]P.G.-J.-C. and D.K.C. contributed equally to this work.

[2]To whom correspondence should be addressed. E-mail: pgolshani@mednet.ucla.edu.

This article contains supporting information online at www.pnas.org/lookup/suppl/doi:10.1073/pnas.1309207110/-/DCSupplemental.

well-characterized receptive field properties with high selectivity to specific stimuli (18), permitting detailed examinations of neural responses to sensory stimuli. Conditional *Pten* deletion was achieved by generating mice in which Cre recombinase, driven by the *alpha-calcium/calmodulin kinase II* (*CaMK2*) promoter, excised one or both copies of *Pten* from forebrain pyramidal neurons (*Methods*). In these mice, Cre expression was restricted to pyramidal neurons in the extragranular layers and expression turned on just before the fourth postnatal week of age (Fig. S1), the peak period of experience-dependent plasticity in the visual cortex (19). By turning on Cre expression and deleting *Pten* at this age, the earlier events of neural differentiation, migration, and cortical lamination proceed normally. A second advantage of this approach is that Cre is not expressed in cortical layer 4 or the lateral geniculate nucleus of the thalamus (Fig. S1), preserving the function of the antecedent input to L2/3 pyramidal neurons.

SK_{Ca} Channel-Dependent Decrease in Intrinsic Excitability in *Pten* Mutants. To examine whether the intrinsic excitability of cortical neurons is altered by single-copy *Pten* deletion, we performed whole-cell recordings from L2/3 pyramidal neurons in slices of the visual cortex from 6-wk-old *CaMK2-Cre*$^{+/-}$;*Pten*$^{+/loxP}$ mice and controls. *Pten* mutant neurons fired fewer action potentials than control neurons to equivalent current step injections (Fig. 1 *A* and *B*) [control ($n = 47$), *Pten*$^{+/-}$ ($n = 33$); $P < 0.05$, two-way ANOVA, Bonferroni post hoc test]. Mutant neurons were also characterized by decreased input resistance ($P = 0.0053$) and an increase in the amplitude of the action potential after hyperpolarization (AHP; $P = 0.0045$), as measured 25 ms after action potential onset (Fig. 1 *C*–*E*). Resting membrane potential, threshold, membrane time constant, action potential amplitude, and half-width were not significantly changed in *Pten*$^{+/-}$ mice relative to controls (Table S1). These data indicate that single-copy loss of *Pten* significantly decreases the intrinsic excitability of pyramidal neurons.

Because a large component of the action potential after hyperpolarization is mediated by calcium-dependent conductances (20, 21), we examined whether these conductances were enhanced in *Pten* mutant neurons. In the presence of the intracellular calcium chelator 1,2-Bis(2-aminophenoxy)ethane-*N*,*N*,*N*′,*N*′-tetraacetic acid (BAPTA; 20 mM), the number of action potentials elicited per current step and measures of input resistance were not different between *Pten*$^{+/-}$ and control neurons (control, $n = 8$; *Pten*, $n = 8$; Fig. 2 *A* and *B*), indicating that changes in calcium-activated conductances play a significant role in diminishing the excitability of *Pten*$^{+/-}$ neurons. Large-conductance calcium-activated potassium channel (BK_{Ca}) and small-conductance calcium-activated potassium channel (SK_{Ca}) are the main subtypes of calcium-dependent potassium conductances in cortical neurons. To examine whether the observed decrease in intrinsic excitability is due to altered BK_{Ca} or SK_{Ca} conductances we bath-applied the BK_{Ca} antagonist paxilline (5 μM) or the SK_{Ca} antagonist apamin (200 nM). In the presence of apamin, measures of the intrinsic excitability of pyramidal neurons, input resistance, and AHP amplitude were indistinguishable in *Pten* heterozygous neurons ($n = 19$) and drug-treated controls ($n = 27$) (Table S1 and Fig. 2 *C*–*F*). Notably, paxilline did not change these measures (Table S1). Western blot of protein isolated from L2/3 of the primary visual cortex showed an approximately threefold increase in SK2 subunit expression in *Pten*$^{+/-}$ mice relative to controls (Fig. 2 *G* and *H*). Taken together, these data show that decreased dosage of PTEN in cortical pyramidal neurons decreases intrinsic excitability by increasing the expression of SK_{Ca} channels, thereby increasing total SK_{Ca} conductances.

***Pten* Haploinsufficiency Reduces Visually Evoked Firing Rates but Does Not Alter Tuning.** Sensory-processing abnormalities are considered by many to be an important feature of autism (22). To examine whether the decrease in intrinsic excitability that we see in acute cortical slices impacts cortical sensory processing, we recorded visually evoked responses of L2/3 pyramidal neurons in loose cell-attached and whole-cell mode. Presumptive fast spiking interneurons were excluded from analysis based on spike waveform (ref. 23; *Methods*). Patch micropipettes were targeted to neuronal somas under visual guidance using the "shadow patch" technique (24). Recordings were made in 4- to 8-wk-old mice. From 29 control mice, we recorded 38 visually responsive and 13 nonresponsive pyramidal neurons. From 11 homozygous mutant mice (*CaMK2-Cre*$^{+/-}$; *Pten*$^{loxP/loxP}$; referred to hereafter as *Pten*$^{-/-}$) we recorded 18 visually responsive and 11 nonresponsive pyramidal neurons. From 11 heterozygous mutant mice (*CaMK2-Cre*$^{+/-}$; *Pten*$^{+/loxP}$; referred to hereafter as *Pten*$^{+/-}$) we recorded 17 visually responsive and 8 nonresponsive pyramidal neurons.

To examine how *Pten* copy number impacts the tuning properties of cortical pyramidal neurons, we presented sine wave drifting gratings at six orientations (12 directions) at a range of spatial frequencies for each cell. Peak evoked firing rates at the optimal direction and spatial frequency were significantly reduced in *Pten*$^{+/-}$ and *Pten*$^{-/-}$ mice compared with controls (Fig. 3 *A* and *B*; one-way ANOVA, $P = 0.0013$; Dunn's posttest $P < 0.05$ control vs. *Pten*$^{+/-}$, control vs. *Pten*$^{-/-}$). Notably, we found no

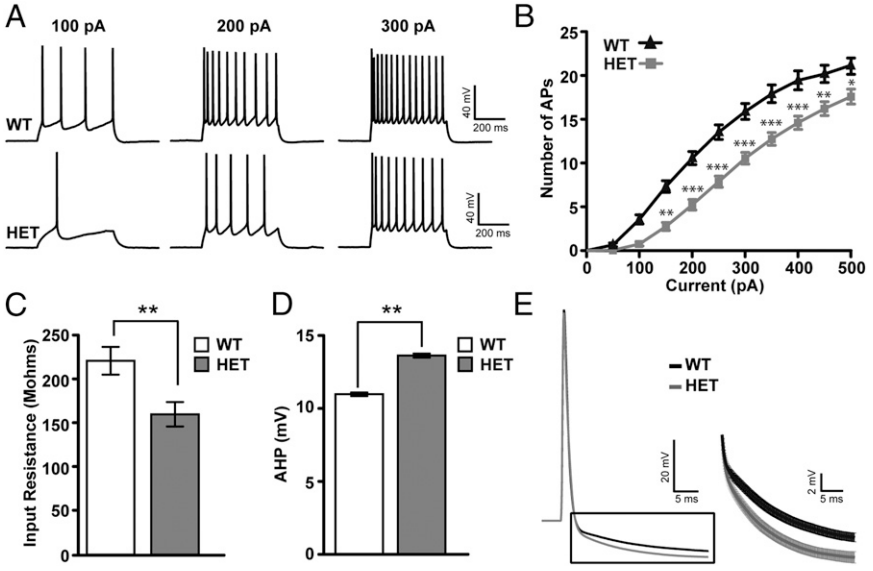

Fig. 1. Intrinsic excitability is altered by *Pten* mutation. (*A*) Example voltage traces elicited by current injection in a L2/3 pyramidal neuron from a control and *Pten* heterozygote (HET) mouse in acute slice preparations. (*B*) Intensity–Frequency (I-F) plot in response to somatic current injection (10 steps of 50 pA, 500 ms duration) in control and *Pten*$^{+/-}$ (HET) neurons. Note the decreased firing rate in HET neurons. Two-way ANOVA test, Bonferroni post hoc test (*$P < 0.05$, **$P < 0.01$, ***$P < 0.001$). (*C*) Input resistance measured in pyramidal neurons of cortical slices taken from control (white bar) and HET (gray bar) mice. Note the decreased input resistance in HET neurons (Student *t* test, $P = 0.0053$). (*D*) Action potential after-hyperpolarization (AHP) measurements in control (white bar) and HET (gray bar) neurons. Note the increased AHP in HET neurons measured 25 ms after action potential onset (Student *t* test, $P = 0.0045$). (*E*) (*Left*) Action potential average (30 ms) from control (black trace) and HET (gray trace) neurons. (*Right*) Average of AHP traces from both genotypes. Note the increased AHP in the HET trace (gray) compared with control trace (black). In all traces, error bars indicate SEM.

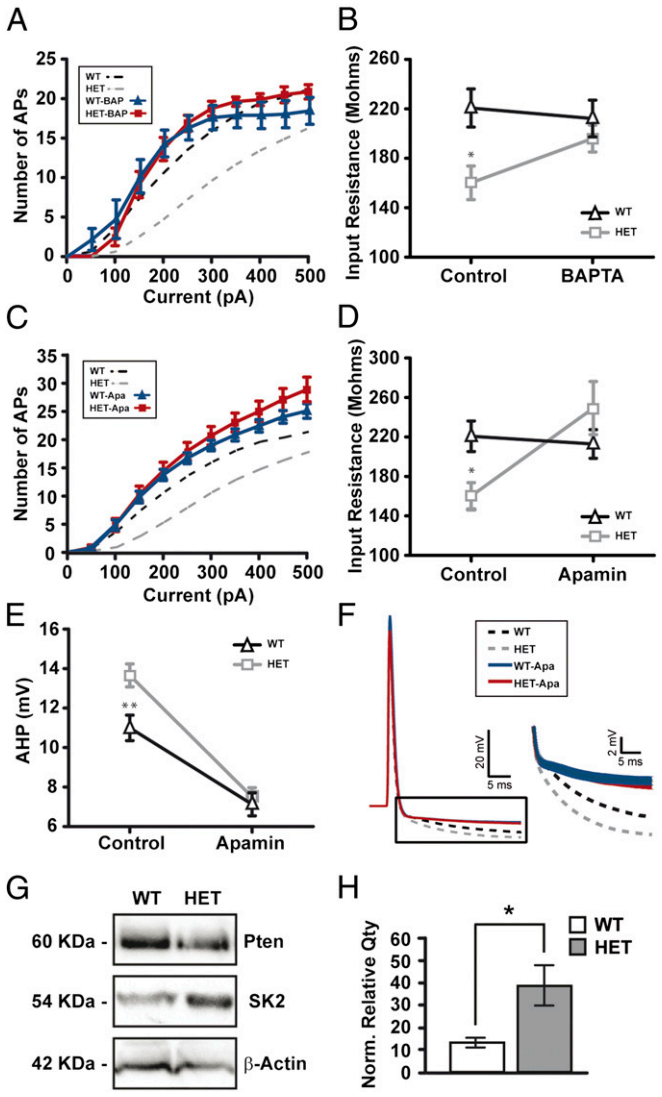

Fig. 2. Calcium-mediated conductances are responsible for the decrease in intrinsic excitability. (*A*) I-F plots in response to somatic current injection in control and *Pten*$^{+/-}$ (HET) neurons in presence of BAPTA (20 mM). Note there are no significant differences in firing rate in control–BAPTA (blue trace) versus *Pten* HET–BAPTA (red trace) neurons. Dotted lines represent control situation. (*B*) Input resistance recovery after BAPTA application. Note how the differences in IR are corrected with BAPTA in HET neurons (gray trace) without affecting control neurons (black trace). ANOVA test, Bonferroni post hoc test (*$P < 0.05$). (*C*) I-F plot in response to somatic current injection in control and HET neurons in presence of apamin (200 nM). Note there are no significant differences in firing rate between control–apamin (blue trace) and *Pten* HET–apamin (red trace) neurons after bath application of apamin. Dotted lines represent control situation. (*D*) Input resistance recovery after apamin bath application. Note how the differences in IR are corrected with apamin in HET neurons (gray trace) without affecting control neurons (black trace). ANOVA test, Bonferroni post hoc test (*$P < 0.05$). (*E*) No differences in AHP after SK_{Ca} channel blockade. Apamin decrease AHP in control (black trace) and HET (gray trace) neurons, suppressing previous differences in control situation. ANOVA test, Bonferroni post hoc test (**$P < 0.01$). (*F*, *Left*) Action potential average (30 ms) from control–apamin (blue trace) and *Pten* HET–apamin (red trace) neurons. (*F*, *Right*) Resized plot of boxed region showing average AHP traces from both genotypes. Note the same decreased AHP in control vs. HET. Dotted lines represent control situation. (*G*) Representative Western blot of cortical protein extracts made from control (WT) and *Pten* HET mice. Immunoblot was probed with PTEN and SK2 antibodies, as well as β-actin as a loading control. (*H*) Quantification of PTEN and SK2 proteins. Densitometry values indicate relative expression of PTEN and SK2 proteins, normalized to β-actin. (*Pten* HET: n = four mice; control; n = three mice; $P < 0.05$ Mann Whitney). In all traces, error bars indicate SEM.

significant difference in firing rates between *Pten*$^{+/-}$ and *Pten*$^{-/-}$ neurons. Spontaneous firing rates were unaffected by *Pten* deletion (Fig. 3*B*, $P = 0.87$, one-way ANOVA). Remarkably, receptive field tuning was preserved despite the decrease in evoked firing rates; indices of orientation selectivity, direction selectivity, and orientation bandwidth were all normal (Fig. 3 *C*–*E*; orientation selectivity: $P = 0.42$, one-way ANOVA; direction selectivity: $P = 0.91$, one-way ANOVA; bandwidth: $P = 0.66$, one-way ANOVA). Fig. 3*F* shows the average baseline-subtracted firing rates in control, *Pten*$^{+/-}$, and *Pten*$^{-/-}$ mice in which the peak response of all neurons has been circularly rotated to a 90° orientation preference. The reliability of action potential firing to the preferred visual stimulus was not different in *Pten*$^{+/-}$ ($n = 17$) and controls ($n = 38$) (Fig. S2*A*; $P = 0.62$). *Pten*$^{+/-}$ neurons fired fewer bursts than control neurons (as measured by the proportion of interspike intervals ranging from 5 to 15 ms), although bursts constituted were rare in both controls and *Pten*$^{+/-}$ (Fig. S2*B*). The mean visually evoked firing rate to the preferred stimulus was not different in *Pten* mutant ($n = 8$) and control neurons ($n = 8$) with high baseline firing rates (putative interneurons), (Fig. S2*C*; $P = 0.95$). These measures show that single- or double-copy loss of *Pten* equally decrease the gain of visually evoked spike output in L2/3 without altering the fundamental tuning properties of these neurons.

Dendritic Growth Is Not Altered in L2/3 Pyramidal Neurons in *Pten* Mutant Mice. Conditional double-copy loss of *Pten* induces apical dendritic growth and new spine formation in L2/3 pyramidal neurons (7). To determine if single-copy loss also altered dendrite size, we imaged the full dendritic structure of a subset of those cells from which we obtained in vivo whole-cell recordings (control, $n = 6$; *Pten*$^{+/-}$, $n = 5$). The internal solution of our patch pipettes contained Alexa dye, which passively filled these neurons, permitting us to fully image their dendritic structure in vivo (compare Fig. 4 *A* and *D* and Fig. S3). We found no changes in apical dendrite length or tortuosity in *Pten*$^{+/-}$ mice (terminal tip length, control: 80 ± 36 μm; *Pten*$^{+/-}$: 82 ± 37 μm; $P = 0.9$; tortuosity, control: 1.16 ± 0.1; *Pten*$^{+/-}$: 1.13 ± 0.05; $P = 0.22$). Sholl analysis also did not show a significant difference in dendritic complexity ($P > 0.05$ at all radii when corrected for multiple comparisons) (Fig. S3). Thus, the spiking deficit we observe in *Pten*$^{+/-}$ neurons is not correlated with gross changes in dendritic structure. These findings support an emerging view in which PTEN's regulation of neural structure and function are mechanistically distinct (25).

Visually Evoked Subthreshold Responses Are Normal in *Pten* Mutant Mice. Reductions in sensory evoked action potential output could be caused by altered synaptic transmission (8) and/or dendritic integration (26). To examine these issues, we measured visually evoked subthreshold modulations in membrane potential (27), which report the integrated somatic response to synaptic activity. Notably, synaptic potentials measured at the soma are spatially and temporally filtered and amplified by intrinsic dendritic conductances (26). Two measures of subthreshold responses to visual stimulation were made: *i*) the direct current (DC or F0) response, which measures the average subthreshold response to each visual stimulus, and *ii*) the alternating current (AC or F1) response, which measures the subthreshold response to each cycle of the drifting grating stimulus that we used (28) (Fig. 4 *B*, *E*, *C*, and *F*). In control neurons ($n = 13$ cells in 12 mice), mean depolarization of the membrane potential (DC) and amplitude of the cycle-averaged membrane potential response (AC) were tuned for stimulus orientation (Fig. 4*G*). DC and AC measurements in *Pten* homozygous and heterozygous mutant neurons were not significantly different ($P > 0.05$); we therefore pooled them to increase statistical power. These measures in *Pten* mutants ($n = 11$ cells in eight mice) were not different from controls at any orientation (for all orientations, see Fig. 4*G*, orange line. At optimal orientation for spiking, DC: control = 5.4 ± 3.9 mV; *Pten* mutants = 5.6 ± 2.4 mV, $P = 0.64$, AC:

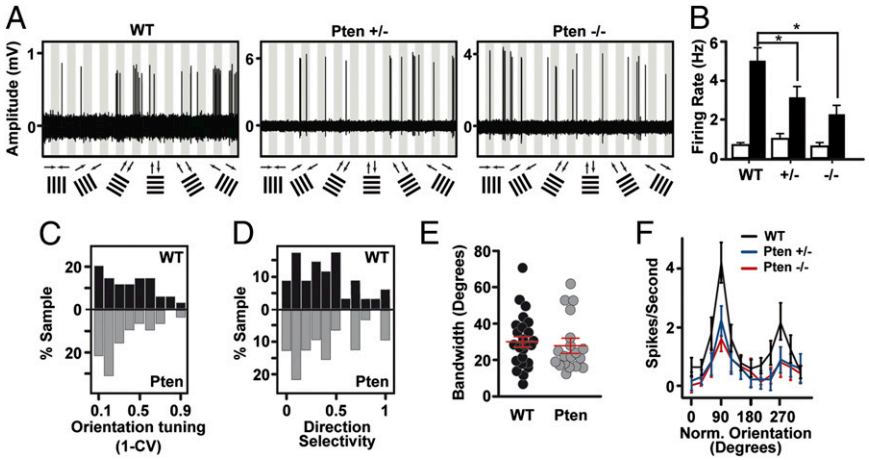

Fig. 3. Single- and double-copy loss of *Pten* decrease evoked firing rates in vivo without altering tuning. (*A*) Example traces of visually evoked responses of a neuron in control, *Pten*$^{+/-}$, and *Pten*$^{-/-}$ mice. Recordings were made in loose cell-attached mode. Drifting gratings were presented in 12 directions, shown at the bottom of each panel. Each gray bar represents 3 s of visual stimulation. White bars are responses to a gray screen. (*B*) Spontaneous (white bar) and peak evoked (black bar) firing rates in control and mutant mice. (*C*) Distribution of orientation tuning preferences in control (black bars) and *Pten* mutant (gray bars) mice (homozygous and heterozygous mutants are pooled for this panel and for *D* and *E*). Tuning is measured as 1 minus circular variance. (*D*) Distribution of direction selectivity indices. (*E*) Distribution of bandwidth measurements in control (black circles) and mutant (gray circles) mice. Mean and SEM are shown in red. (*F*) Average background subtracted spike rate plotted for all orientations and directions for control (black), *Pten*$^{+/-}$ (blue), and *Pten*$^{-/-}$ (red) mice. Tuning for all cells has been circularly rotated so that all cells have best tuning at 90°(vertical bars drifting to the right). Note the preservation of direction and orientation selectivity despite the decreased firing rate in the mutant neurons.

control = 9.0 ± 4 mV; *Pten* mutants = 7.2 ± 2.7 mV, $P = 0.37$). Orientation tuning of the F0 and F1 (DC and AC) subthreshold responses was not different between controls and PTEN mutants (Fig. 4*H*). Furthermore, action potential threshold recorded in vivo was not different between the two groups (control = −40.1 ± 4.0 mV; *Pten* mutants = −37.5 ± 4.4 mV, $P = 0.1$). Finally, *Pten* mutant neurons recorded in whole-cell mode in vivo showed increase in the amplitude of the spike AHP as measured 15 ms after spike onset (control: 1.55 ± 0.42 mV; *Pten* mutants: 3.16 ± 0.35 mV; $P = 0.012$; Fig. S4). These data show that subthreshold voltage modulations, which are synaptic potentials, filtered and amplified by dendritic conductances, are similar in mutant and control neurons.

Discussion

Approximately 7% of macrocephalic children with autism have single-copy mutations (3). Previous studies have identified cortical dendritic and synaptic changes induced following double-copy loss of *Pten* (5, 7, 8), yet far less is known about how single-copy loss of *Pten*, as would occur with inherited or de novo mutations in humans (29), impacts the structure and function of the nervous system.

Here, we show that single-copy loss of *Pten* in cortical pyramidal neurons increases SK_{Ca} conductances, causing a decrease in intrinsic excitability. In vivo, this causes a significant reduction in sensory-evoked firing rates but does not change receptive field tuning. Notably, the change in in vivo firing rates was found in both heterozygous mice, in which dendrites did not grow, and in homozygous mice, where dendritic growth is pronounced. We found no significant change in spontaneous firing rates of cells, likely because spontaneous firing rates in control L2/3 visual cortical neurons were already very low, creating a floor effect. Our findings provide further evidence that PTEN's regulation of cellular morphology and physiology is mechanistically separable (25).

It is possible that changes to the expression levels of other potassium channels (25) or inhibitory conductances (30) could play a role in the changes of response magnitude seen in vivo, although the decrease in intrinsic excitability was entirely rescued by SK_{Ca} channel blockade. Increased SK_{Ca} channel expression could also potentially decrease the size of excitatory synaptic potentials at the spine through activation by calcium entry through NMDA receptors or voltage-gated calcium channels (31, 32).

In the visual system, gain modulation adjusts neural responsiveness without impairing selectivity and is used to scale cortical network function in a contrast-dependent manner (33). Changes in input–output functions adjust firing rates to enhance coding of dynamic visual scenes where luminance, spatial frequency, and contrast often change over many orders of magnitude. Higher-level brain regions compare the outputs of these lower-level sensory neurons to compute perceptual decisions (34). Impairments in low-level gain modulation, as seen here, would therefore be expected to degrade sensory perception in noisy or ambiguous contexts. Changes in gain modulation are increasingly found to drive experience-dependent plasticity in the normal cortex (35, 36), and there is growing recognition that deficits in gain modulation and its plasticity underlie the pathophysiology of some neurodevelopmental diseases, including autism (37, 38). The lower visually evoked firing rates in the primary visual cortex *Pten*$^{+/-}$ mice may result in weakened recruitment of downstream secondary visual cortical and nonvisual areas, degrading sensory processing.

On a more fundamental level, our data showing that changes in intrinsic excitability are due to changes in SK_{Ca} channels identify potassium channelopathy as a potential underlying cause of cortical dysfunction resulting from *PTEN* haploinsufficiency. Future studies in model animals will be needed to determine if modulation of SK_{Ca} channels can potentially rescue sensory dysfunction and social behavioral deficits.

Methods

Our experiments were approved by the University of California Los Angeles Office for Protection of Research Subjects and the Chancellor's Animal Research Committee.

Animals. The generation of mice carrying a conditional *Pten* loxP/loxP allele flanking exon 5, which encodes PTEN's phosphatase domain, has been described previously (39). Mice with a *Pten*$^{loxp/loxp}$ allele flanking exon 5 were crossed with mice carrying an *alpha-CaMK2*-driven *Cre* transgene (*Cre*$^{+/-}$) (T-50 line), as described in ref. 7. Resulting mice were intercrossed to generate *alpha-CaMK2–Cre*$^{+/-}$; *Pten*$^{loxp/loxp}$ and *alpha-CamKII–Cre*$^{+/-}$; *Pten*$^{loxp/+}$ mice. All mice were in a C57Bl6 background, backcrossed at least seven generations. Control mice were littermates that had no Cre expression. To determine where Cre is expressed in the visual pathway and when its expression begins, we crossed *alpha-CaMK2–Cre*$^{+/-}$ mice with mice expressing a floxed red fluorescent protein reporter gene (tdTomato) that is knocked into the Rosa26 locus (AI9 line of mice from Allen Brain Institute; Jackson Laboratories 007909). Sections were cut at 40-μm thickness and imaged with two-photon excitation. Cell counts were made using Neurolucida software. Fig. S1 plots the change in cortical expression as a function of age in L2/3 of the primary visual cortex.

Surgery for in Vivo Physiology. Four- to eight-week-old male or female mice were anesthetized with chlorprothixene (5 mg/kg) and urethane (0.5 g/kg). A 2- to 3-mm craniotomy was performed over the primary visual cortex. Supplemental doses of urethane (0.1–0.2 mg/kg) were administered when the animal showed signs of arousal from anesthesia. At the time of the recordings, *Pten* mutant animals were indistinguishable in appearance from

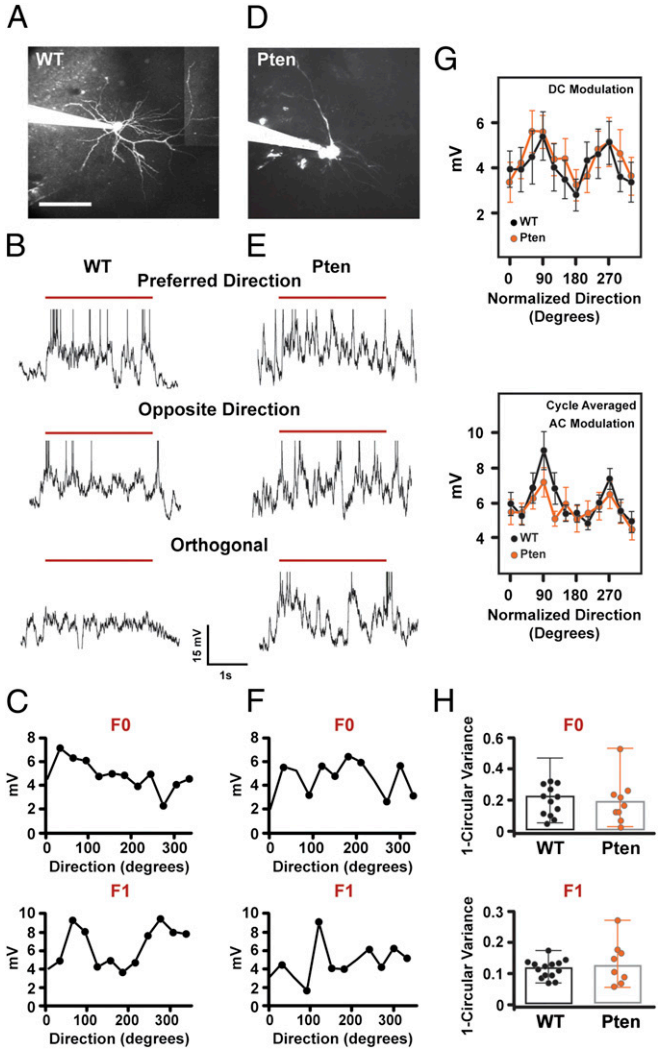

Fig. 4. Tuning of evoked subthreshold membrane depolarization is unaffected by *Pten* mutation. (*A* and *D*) Maximum-intensity projection of a L2/3 pyramidal neuron from a control mouse (*A*) and *Pten* HET mouse (*D*) filled with Alexa 594 in whole-cell patch configuration and imaged with two-photon laser-scanning microscopy. The patch pipette is seen entering the image from the *Left*. (Scale bar, 100 μm.) (*B* and *E*) Single-trial membrane potential (MP) responses elicited by 3 s of visual stimulation with sine wave-drifting gratings (red line represents visual stimulus with the grating) at the preferred, opposite, and orthogonal direction from a whole-cell recording from a control (*B*) and *Pten* HET (*E*) L2/3 neuron. Spikes have been truncated for display purposes. (*C* and *F*) Average DC (F0) (*Upper*) and AC (F1) (*Lower*) modulation of the membrane potential for the control neuron (*C*) and the *Pten* HET neuron (*F*). (*G*) DC (F0) (*Upper*) and AC (F1) (*Lower*) modulation of subthreshold responses as a function of direction for control (black) and mutant (orange) neurons. Plots are mean and SE. Peak orientation is normalized to 90° for all cells. (*H*) Distribution of orientation selectivity indices for the DC (F0) (*Upper*) and AC (F1) (*Lower*) modulations for control and *Pten* mutant neurons. The bar shows the median OSI, and error bars represent the range.

their littermates and required similar doses of anesthesia for the experiments. A circular glass coverslip was positioned such that it covered most of the craniotomy but allowed access for micropipettes to penetrate the brain; the coverslip was fixed to the skull with dental cement. A recording well was made out of dental cement. A stainless steel bar attached to a custom-made head holder was used to immobilize the head for recordings. A silver chloride ground electrode was implanted over the cerebellum.

In Vivo Cell-Attached and Whole-Cell Recordings. Micropipettes were pulled on Sutter Instruments P-97 pipette puller to a resistance of 5–7 MΩ, when filled with an internal solution containing (in mM): KGluc 105, KCl 30, Hepes 10, phosphocreatine 10, ATP-Mg 4. GTP 0.3, Alexa-594 0.01–0.05. The pressure in the recording pipette was set at 300 mbars as the microelectrode penetrated the brain. Pressure was decreased to 50–70 mbars as the pipette was guided to L2/3 and then reduced to 20 mbars. In vivo two-photon imaging was performed with a custom-made two-photon microscope and ScanImage software (40) using a Ti-Sapphire laser at 800 nm and a 40× 0.8 numerical aperture (NA) Zeiss water-immersion objective or a 16× 0.9 NA water-immersion objective. Neuronal somata could be clearly visualized as silhouettes on the background of neuropil stained by the extruded Alexa-594. The pipette was placed against the soma, and this placement was confirmed by accumulation of the Alexa-594 against the soma as well as an increase in the resistance of the pipette. Negative pressure (up to −100 mbars) was then applied. In vivo cell-attached or whole-cell recordings were performed with an Axoclamp 2A amplifier (Axon Instruments). Traces were low-pass-filtered at 5 kHz and digitized at 10 kHz, using NIDAQ cards (National Instruments) running under the WinEDR and WinWCP Strathclyde Electrophysiology Software. Cell-attached recordings of action potential firing were performed in current clamp mode when a GΩ seal could not be obtained. When a GΩ seal was obtained, further negative pressure was applied to gain whole-cell access. No junction potential subtraction was performed. Cells with a resting membrane potential below −60 mV were included. The cell's anatomy was reconstructed in three dimensions by performing multiple overlapping image stacks at 2–4 μm using Neurolucida. Tortuosity was measured as a ratio of the length along the distance of the dendrite from base to tip, divided by the straight line distance from base to the tip of the dendrite (actual length/straight line distance). Terminal tip lengths were measured as the lengths of dendrite segments from terminal tip to nearest branch point. Sholl analysis was performed by on the *Z* stack projections of Neurolucida reconstructions by counting the number of intersections of dendrites with concentric rings spaced every 25 μm. Statistical significance was measured using a two-tailed *t* test comparing controls vs. $Pten^{+/-}$. For Sholl analysis, *P* values were corrected for multiple comparisons.

Membrane potential responses were filtered with a 5-ms median filter to remove action potentials from the trace; three to four repeats of the same visual presentation were averaged. To calculate AC modulation amplitude, responses were cycle-averaged by averaging six consecutive 500-ms epochs of a 3-s visual presentation (2 Hz temporal frequency). Cells were considered nonresponsive if the mean minus SD of the baseline subtracted firing rate was less than zero across all orientations. In cell-attached mode, cells were considered fast spiking interneurons if the peak to trough of the action potential waveform was less than 0.7 ms. In whole-cell mode cells were considered fast spiking interneurons if the half-width of the action potential was less than 0.7 ms. These cells were not included in the analysis. Rare cells with baseline firing rates greater than 3 Hz were also not included in the analysis as they are likely inhibitory interneurons (23).

Slice Whole-Cell Recordings. Recordings were made from 6-wk-old mice. The brain was removed and placed into ice-cold cutting solution in Mm: sucrose 222, D-glucose 11, $NaHCO_3$ 26, NaH_2PO4 1, KCl 3, $MgCl_2$ 7, $CaCl_2$ 0.5, aerated with 95% O_2, 5% CO_2. Three hundred-micrometer coronal slices of the visual cortex were cut with a Leica VT1000S Vibratome. Slices were allowed to recover at 37 °C in artificial cerebrospinal fluid (ACSF) in mM: NaCl 124, KCl 2.5, $NaHCO_3$ 26 NaH_2PO_4 1.25, D-glucose 10, sucrose 4,$CaCl_2$ 2.5, $MgCl_2$ 2, aerated with 95% O_2, 5% CO_2. Whole-cell recordings of L2/3 neurons were made in current clamp mode using a Multiclamp (Molecular Devices) patch clamp amplifier under visual guidance using differential interference contrast (DIC) optics with an Olympus BX51 microscope. Recordings were performed at 33–35 °C. The internal solution contained (in mM): KGluc 115, KCl 20, Hepes 10, phosphocreatine 10, ATP–Mg^{2+} 4, GTP–Na^{+} 0.3. Micropipettes were 3–5 MΩ in resistance. Series resistance was below 30 MΩ and fully compensated in current clamp mode. In calcium chelation experiments, BAPTA (20 mM) was included in the internal solution. Paxilline (5 μM) or apamin (200 nM) were added to the ACSF when corresponded. Fast spiking interneurons were excluded from analysis. To analyze all action potential parameters, we injected the minimum current intensity to evoke one action potential. Input resistance was calculated as the slope of the linear fit of the voltage–current plot generated from a family of positive and negative current injections (−100 to +100 pA at 25-pA intervals, 500 ms in duration). For analysis we use Axograph X software (Molecular Devices).

Western Blots. Brains from 1-mo-old wild-type and $Pten^{+/-}$ mice were dissected in ice-cold cutting solution, and 300-μm slices were cut as described above. Microdissection of the visual cortex was performed, and samples

were kept on ice or stored at −20 °C until further processing. Tissue was then homogenized in RIPA buffer, followed by centrifugation at 4 °C for 10 min at 16,060 × *g*. The resultant supernatant was obtained, and proteins were fractioned by SDS/PAGE. Immunoblots were probed with rabbit anti-K_{Ca}2.2 (SK2) (Alomone Labs, 1:250), rabbit anti-PTEN C-Term, clone Y184 (Millipore, 1:500), and mouse anti–β-actin, clone AC-15 (Sigma-Aldrich, 1:250), followed by appropriate IgG conjugated with horseradish peroxidase as a secondary antibody. SuperSignal West Pico Chemiluminescent Substrate (Thermo Scientific) was applied for protein detection. Imaging and densitometric quantification was done using ChemiDoc XRS+ System (Bio-Rad). The membranes were stripped with Restore Western Blot Stripping Buffer (Thermo Scientific), and each antibody was applied separately to the same membrane for better appreciation of individual bands. Two replicates were made for each mouse to confirm validity of the results. Relative protein levels were calculated by normalizing relative quantities of both PTEN and SK2 to β-actin loading controls, and significance was determined by using a Mann–Whitney test.

Analysis. The global orientation selectivity index (OSI) was calculated as 1 minus circular variance (41, 42). Direction selectivity and bandwidth were calculated as in ref. 18. Briefly, direction selectivity was calculated after subtracting baseline firing rate as (spike rate at preferred orientation minus spike rate at opposite orientation)/(the sum of the spike rates at both orientations). Orientation bandwidth, a local measure of orientation selectivity, was measured at half-width, half-height after fitting a sum of two Gaussians (18). The reliability of the action potential firing to the visual stimulus of preferred direction was calculated by measuring the Fano factor (variance/mean) of the mean firing rate across multiple presentations of the stimulus. The tendency of burst firing was measured by calculating the proportion of interspike intervals that fell below 5–15 ms.

Statistics. To examine significance across multiple comparisons, a one-way ANOVA (Kruskal–Wallis) was first performed, followed by Dunn's posttest. For comparisons of two data sets, unpaired *t* tests were used. Error bars in all figures are SEM.

ACKNOWLEDGMENTS. We thank Dr. Sandra Kuhlman for her help and advice during the analysis of the data. We also thank Dr. Mathias Groszer, Dr. Tom Otis, Dr. Dario Ringach, and Dr. Larry Zipursky for their critical discussions of the data. This work was supported by National Institutes of Health K08 Grant NS-056210 and NIH R01 Grant MH-101198 (to P.G.) and NIH R01 Grant MH082935 (to J.T.T. and P.G.). P.G.-J.-C. was supported by postdoctoral Fellowship EX2009-0750 from the Spanish Ministry of Education, Culture and Sport.

1. Varga EA, Pastore M, Prior T, Herman GE, McBride KL (2009) The prevalence of PTEN mutations in a clinical pediatric cohort with autism spectrum disorders, developmental delay, and macrocephaly. *Genet Med* 11(2):111–117.
2. Herman GE, et al. (2007) Increasing knowledge of PTEN germline mutations: Two additional patients with autism and macrocephaly. *Am J Med Genet A* 143(6): 589–593.
3. McBride KL, et al. (2010) Confirmation study of PTEN mutations among individuals with autism or developmental delays/mental retardation and macrocephaly. *Autism Res* 3(3):137–141.
4. O'Roak BJ, et al. (2012) Multiplex targeted sequencing identifies recurrently mutated genes in autism spectrum disorders. *Science* 338(6114):1619–1622.
5. Kwon CH, et al. (2006) Pten regulates neuronal arborization and social interaction in mice. *Neuron* 50(3):377–388.
6. Page DT, Kuti OJ, Prestia C, Sur M (2009) Haploinsufficiency for Pten and Serotonin transporter cooperatively influences brain size and social behavior. *Proc Natl Acad Sci USA* 106(6):1989–1994.
7. Chow DK, et al. (2009) Laminar and compartmental regulation of dendritic growth in mature cortex. *Nat Neurosci* 12(2):116–118.
8. Xiong Q, Oviedo HV, Trotman LC, Zador AM (2012) PTEN regulation of local and long-range connections in mouse auditory cortex. *J Neurosci* 32(5):1643–1652.
9. Tabuchi K, et al. (2007) A neuroligin-3 mutation implicated in autism increases inhibitory synaptic transmission in mice. *Science* 318(5847):71–76.
10. Peça J, et al. (2011) Shank3 mutant mice display autistic-like behaviours and striatal dysfunction. *Nature* 472(7344):437–442.
11. Splawski I, et al. (2004) Ca(V)1.2 calcium channel dysfunction causes a multisystem disorder including arrhythmia and autism. *Cell* 119(1):19–31.
12. Strauss KA, et al. (2006) Recessive symptomatic focal epilepsy and mutant contactin-associated protein-like 2. *N Engl J Med* 354(13):1370–1377.
13. Alarcón M, et al. (2008) Linkage, association, and gene-expression analyses identify CNTNAP2 as an autism-susceptibility gene. *Am J Hum Genet* 82(1):150–159.
14. Arking DE, et al. (2008) A common genetic variant in the neurexin superfamily member CNTNAP2 increases familial risk of autism. *Am J Hum Genet* 82(1):160–164.
15. Sanders SJ, et al. (2012) De novo mutations revealed by whole-exome sequencing are strongly associated with autism. *Nature* 485(7397):237–241.
16. Raab-Graham KF, Haddick PC, Jan YN, Jan LY (2006) Activity- and mTOR-dependent suppression of Kv1.1 channel mRNA translation in dendrites. *Science* 314(5796):144–148.
17. Groszer M, et al. (2001) Negative regulation of neural stem/progenitor cell proliferation by the Pten tumor suppressor gene in vivo. *Science* 294(5549):2186–2189.
18. Niell CM, Stryker MP (2008) Highly selective receptive fields in mouse visual cortex. *J Neurosci* 28(30):7520–7536.
19. Gordon JA, Stryker MP (1996) Experience-dependent plasticity of binocular responses in the primary visual cortex of the mouse. *J Neurosci* 16(10):3274–3286.
20. Nelson AB, Krispel CM, Sekirnjak C, du Lac S (2003) Long-lasting increases in intrinsic excitability triggered by inhibition. *Neuron* 40(3):609–620.
21. Bond CT, Maylie J, Adelman JP (2005) SK channels in excitability, pacemaking and synaptic integration. *Curr Opin Neurobiol* 15(3):305–311.
22. Crane L, Goddard L, Pring L (2009) Sensory processing in adults with autism spectrum disorders. *Autism* 13(3):215–228.
23. Ma WP, et al. (2010) Visual representations by cortical somatostatin inhibitory neurons—selective but with weak and delayed responses. *J Neurosci* 30(43):14371–14379.
24. Kitamura K, Judkewitz B, Kano M, Denk W, Häusser M (2008) Targeted patch-clamp recordings and single-cell electroporation of unlabeled neurons in vivo. *Nat Methods* 5(1):61–67.
25. Sperow M, et al. (2012) Phosphatase and tensin homologue (PTEN) regulates synaptic plasticity independently of its effect on neuronal morphology and migration. *J Physiol* 590(Pt 4):777–792.
26. London M, Häusser M (2005) Dendritic computation. *Annu Rev Neurosci* 28:503–532.
27. Gillespie DC, Lampl I, Anderson JS, Ferster D (2001) Dynamics of the orientation-tuned membrane potential response in cat primary visual cortex. *Nat Neurosci* 4(10):1014–1019.
28. Carandini M, Ferster D (2000) Membrane potential and firing rate in cat primary visual cortex. *J Neurosci* 20(1):470–484.
29. O'Roak BJ, et al. (2012) Sporadic autism exomes reveal a highly interconnected protein network of de novo mutations. *Nature* 485(7397):246–250.
30. Weston MC, Chen H, Swann JW (2012) Multiple roles for mammalian target of rapamycin signaling in both glutamatergic and GABAergic synaptic transmission. *J Neurosci* 32(33):11441–11452.
31. Bloodgood BL, Sabatini BL (2007) Nonlinear regulation of unitary synaptic signals by CaV (2.3) voltage-sensitive calcium channels located in dendritic spines. *Neuron* 53(2):249–260.
32. Ngo-Anh TJ, et al. (2005) SK channels and NMDA receptors form a Ca2+-mediated feedback loop in dendritic spines. *Nat Neurosci* 8(5):642–649.
33. Rieke F, Rudd ME (2009) The challenges natural images pose for visual adaptation. *Neuron* 64(5):605–616.
34. Heekeren HR, Marrett S, Bandettini PA, Ungerleider LG (2004) A general mechanism for perceptual decision-making in the human brain. *Nature* 431(7010):859–862.
35. Nataraj K, Le Roux N, Nahmani M, Lefort S, Turrigiano G (2010) Visual deprivation suppresses L5 pyramidal neuron excitability by preventing the induction of intrinsic plasticity. *Neuron* 68(4):750–762.
36. Turrigiano G (2011) Too many cooks? Intrinsic and synaptic homeostatic mechanisms in cortical circuit refinement. *Annu Rev Neurosci* 34:89–103.
37. Du W, et al. (2005) Calcium-sensitive potassium channelopathy in human epilepsy and paroxysmal movement disorder. *Nat Genet* 37(7):733–738.
38. Laumonnier F, et al. (2006) Association of a functional deficit of the BKCa channel, a synaptic regulator of neuronal excitability, with autism and mental retardation. *Am J Psychiatry* 163(9):1622–1629.
39. Lesche R, et al. (2002) Cre/loxP-mediated inactivation of the murine Pten tumor suppressor gene. *Genesis* 32(2):148–149.
40. Pologruto TA, Sabatini BL, Svoboda K (2003) ScanImage: flexible software for operating laser scanning microscopes. *Biomed Eng Online* 2:13.
41. Ringach DL, Shapley RM, Hawken MJ (2002) Orientation selectivity in macaque V1: diversity and laminar dependence. *J Neurosci* 22(13):5639–5651.
42. Kerlin AM, Andermann ML, Berezovskii VK, Reid RC (2010) Broadly tuned response properties of diverse inhibitory neuron subtypes in mouse visual cortex. *Neuron* 67(5): 858–871.